








Predictions of the Nancy Grace Roman Space Telescope Galactic Exoplanet Survey. V. Detection Rates of Multiplanetary Systems in High Magnification Microlensing Events

Vito Saggese^{1,2,3} , Étienne Bachelet^{4,5} , Sebastiano Calchi Novati⁵ , Valerio Bozza^{6,3} , Giovanni Covone^{2,3,7} ,
Farzaneh Zohrabi⁸ 

(Leading Authors)

Michael D. Albrow⁹ , Jay Anderson¹⁰ , Charles Beichman¹¹ , David P. Bennett^{12,13} , Aparna Bhattacharya^{12,13},
Christopher Brandon¹⁴, Sean Carey⁵ , Jessie Christiansen⁵ , Alison Crisp¹⁴ , William DeRocco^{12,15} , B. Scott
Gaudi¹⁴ , Jon Hulberg^{16,13,17} , Macy J. Huston¹⁸ , Stela Ishitani Silva¹³ , Eamonn Kerins¹⁹ , Somayeh
Khakpash²⁰ , Katarzyna Kruszyńska²¹ , Casey Lam²² , Jessica R. Lu¹⁸ , Amber Malpas¹⁴ , Arjun Murlidhar¹⁴ ,
Marz Newman⁸ , Greg Olmschenk^{12,13} , Matthew Penny⁸ , Keivan G. Stassun²³ , Alexander P. Stephan²³ ,
Rachel A. Street²¹ , Takahiro Sumi²⁴ , Sean K. Terry^{12,13} , Himanshu Verma⁸ , and Weicheng Zang²⁵ 

(Roman Galactic Exoplanet Survey Project Infrastructure Team)

(Affiliations can be found after the references)

Received ...

ABSTRACT

Context. The Nancy Grace Roman Space Telescope will expand the reach of gravitational microlensing surveys by increasing the number of events monitored and the precision of their light curves.

Aims. We investigate Roman’s ability to detect triple-lens microlensing systems, cases where a foreground star with two bound exoplanets produces detectable anomalies in a microlensing event, using its planned high-cadence observations toward the Galactic bulge.

Methods. We simulate a large set of high-magnification microlensing light curves based on Roman’s expected survey characteristics. A detection criterion, based on a required χ^2 improvement for a two-planet model, is applied to determine whether the second planet can be reliably distinguished from a single-planet (binary-lens) model.

Results. Our simulations show that the majority of two-planet microlensing events would be detectable with Roman. Events in which both planets are relatively massive (planet–star mass ratios of order 10^{-3}), or in which the more massive planet occupies a favorable resonant configuration, produce strong central perturbations, resulting in detection efficiencies of roughly 90%. By contrast, systems with only low-mass planets ($q \sim 10^{-4}$) or with less favorable alignments generate much weaker signals, which often fall below the detection threshold. In general, the planetary mass ratios and the resulting caustic geometry (e.g., central caustic size in resonant versus wide/close orbits) are the dominant factors governing detectability.

Conclusions. Taking into account the expected frequency of planetary systems and the fraction of high-magnification events, we estimate that Roman will detect a high-magnification triple-lens event in approximately 4.5% of multi-planet microlensing events, corresponding to about 64 events over the course of the full survey.

Key words. gravitational lensing: micro – planetary systems: detection

1. Introduction

In the current landscape of exoplanetary science, about six thousands of exoplanets have been discovered to date. However, only about 40% of these are found within multiplanetary systems (NASA Exoplanet Archive 2025), i.e., systems hosting more than one planet. The majority of such systems have been discovered through the transit method (Struve 1952; Seager & Mallén-Ornelas 2003) and radial velocity measurements, through which the first planets around a main-sequence star was discovered (Mayor & Queloz 1995); with the former gaining significant success thanks to wide-field space-based missions such as *CoRoT* (Auvergne et al. 2009), *Kepler* (Borucki et al. 2010), *K2* (Howell et al. 2014) and *TESS* (Ricker et al. 2015). These missions have revealed a rich diversity of exoplanetary architectures and enable statistical studies that, together with refined theoretical models (Lissauer et al. 2011; Fabrycky et al. 2014; Mordasini

et al. 2012), have challenged traditional, static models of in-situ planetary formation, prompting a paradigm shift toward more dynamic theories emphasizing planetary migration and post-formation atmospheric evolution. In addition, planet occurrence is also affected by stellar multiplicity, with tight binaries showing a suppressed planet yield (Sullivan et al. 2025). Looking ahead, the upcoming ESA mission *PLATO* (Rauer et al. 2024), scheduled for launch in 2026 and designed to detect terrestrial planets in the habitable zones of Sun-like stars, will further expand the reach of transit surveys. Among the various techniques for detecting exoplanets, gravitational microlensing plays a uniquely complementary role. Unlike other methods, microlensing is sensitive to planets at wide orbital separations, particularly beyond the snow line, and to free-floating or non-transiting planets that would otherwise remain undetectable (Mroz & Poleski 2023). Moreover, microlensing events allow the detection of planetary systems located at kiloparsec-scale distances, far beyond the

reach of most other techniques. Statistical studies based on microlensing data (Gould et al. 2010; Cassan et al. 2012; Suzuki et al. 2016; Shvartzvald et al. 2017) consistently indicate that such planets are common, with cold Neptunes and super-Earths being particularly abundant. These findings suggest that planetary systems with wide-separation planets may be the rule in our Galaxy, highlighting the importance of microlensing in constructing a complete picture of planetary demographics. The upcoming launch of the *Nancy Grace Roman Space Telescope*¹ (Spergel et al. 2015; Zasowski et al. 2025) will mark a significant advancement in microlensing capabilities. Scheduled to conduct a dedicated microlensing survey toward the Galactic bulge, Roman will improve our sensitivity to distant and cold exoplanets through its wide-field infrared observations (Penny et al. 2019). Roman will provide data to enable an overview of planetary systems across different orbital architectures, thereby bridging the gap between close-in planets detected by transit missions and the more distant planetary populations accessible through microlensing.

To date, a total of 256 planets have been discovered through gravitational microlensing. Despite its potential, detections of multiplanetary systems via this method remain extremely rare due to the intrinsic difficulty of observation and modelling. To date, 11 planets have been discovered within binary systems (Poleski et al. 2014; Gould et al. 2014; Bennett et al. 2016; Han et al. 2017; Bennett et al. 2020; Han et al. 2020; Zang et al. 2021; Han et al. 2021a,b; Kuang et al. 2022; Han et al. 2024), while fewer than a dozen microlensing-detected systems have been confirmed to host multiple planets—all of them being triple systems. OGLE-2006-BLG-109 (Gaudi et al. 2008; Bennett et al. 2010) system is the first double-planet system discovered using gravitational microlensing, with a configuration similar to the Jupiter–Saturn pair in our Solar System. The Saturn-like planet’s orbital motion is even visible in the microlensing light curve, allowing partial constraints on its orbit. OGLE-2012-BLG-0026 (Han et al. 2013; Beaulieu et al. 2016) is a well-characterized system consisting of a solar-mass G-type main-sequence star in the Galactic disk, orbited by two cold gas giant planets; the masses are determined with a precision of 5%. OGLE-2014-BLG-1722 (Suzuki et al. 2018) is a likely two-planet system, consisting of a late-type host star with two cold Saturn-mass planets. It is the first multiple-planet system discovered in a low-magnification microlensing event. Even though there is no detection of parallax or finite-source effects, a Bayesian analysis constrains the planetary masses and separations. OGLE-2018-BLG-1011 (Han et al. 2019) is a two-planet microlensing planetary system with two Jupiter-mass planets orbiting a low-mass star. The event displays a characteristic double-peaked anomaly on its light curve. Bayesian analysis constrains the system at a distance of ~ 7.1 kpc. OGLE-2019-BLG0468 (Han et al. 2022b) is a microlensing system consisting of two giant planets orbiting a G-type star with a mass of $\sim 0.9 M_{\odot}$. The event displays a triple anomaly in its light curve, which is best explained by a triple-lens model. This system expands the known population of cold giant planets beyond the snow line. KMT-2020-BLG-0414 (Zang et al. 2021) is not properly a multi planetary system, it is a triple-lens microlensing system comprising a low-mass host star orbited by an Earth-mass planet and a brown dwarf companion. The system was discovered during a high-magnification ($A_{\max} \sim 1450$) microlensing event, with a planet-to-host mass ratio of $q_2 \sim (0.9\text{--}1.2)10^{-5}$, one of the lowest ever detected via

microlensing. KMT-2021-BLG-1077L (Han et al. 2022a) is a microlensing system composed of a mid-to-late M-dwarf host star orbited by two cold gas giant planets. The system lies in the Galactic bulge at a distance of ~ 8.24 kpc, making it the most distant multi-planetary microlensing system discovered so far. KMT-2022-BLG-1818L (Li et al. 2025) is a microlensing system with a K-dwarf host star orbited by a super-Jupiter and a Saturn-class planet. The super-Jupiter lies on a Jupiter-like orbit, while the Saturn-class planet may be either close-in (~ 0.4 au) or wide (~ 13 au), making it in the latter case the lowest-mass planet known beyond (10 au) in a multiplanet system.

With the advent of Roman, events of this kind are expected to become significantly more common. Roman will provide continuous, high-cadence, high-precision photometric monitoring of millions of stars, leading to a substantial increase in the detection rate of microlensing events. This will enable the detection of weaker signals from low-mass companions orbiting host stars with far greater ease than is possible with current ground-based facilities or *Gaia*. Moreover, its enhanced sensitivity may even allow for the detection of exomoons.

This work is the fifth paper in the RGES yield–forecast series, which models the expected planet discoveries from the Roman microlensing survey. The first study (Penny et al. 2019) established the simulation framework and demonstrated that, under Roman’s nominal design the survey is expected to detect roughly 1.4×10^3 bound exoplanets with masses above $\sim 0.1 M_{\oplus}$. Subsequent analyses extended this framework to free-floating planets (Johnson et al. 2020), predicting ~ 250 detections down to Mars mass when adopting the planet mass function of Cassan et al. (2012), and to exomoons orbiting wide-separation giant planets (Lastovka et al. 2025), for which only of order one detection is expected over the mission lifetime. The fourth paper in the series (Terry et al. 2025) investigated the precision with which the Roman Galactic Exoplanet Survey will be able to measure host-lens masses and distances, demonstrating that the mission will meet its science requirement of achieving 20% precision for at least 40% of detected planet hosts.

In the present study we investigate the capability of Roman to detect microlensing events produced by triple-lens systems composed of a host star and two bound planets. We restrict our analysis to this specific configuration, as the probability of clearly detecting signals from more than three planets in a single event is extremely low due to the increased complexity of caustic structures, overlapping planetary perturbations, and the short duration of anomalies (Shvartzvald & Maoz 2012). Several previous works have numerically investigated the detectability of multiple-planet systems via microlensing. Early studies such as Gaudi et al. (1998) and Han et al. (2001) demonstrated that high-magnification events offer the most favorable conditions for detecting multiple planets, due to the enhanced sensitivity to central caustic perturbations. Subsequent analyses by Chung et al. (2005), Han (2006) further explored the morphology and interaction of caustics in triple-lens geometries.

More recently, Kuang et al. (2023) conducted a detailed numerical study of triple-lens systems modeled after a scaled Solar System analog, consisting of a star, a Jupiter-like planet, and a Saturn-like companion. They demonstrated that under certain geometrical configurations, the planetary signals remain distinguishable, especially when the caustics are well separated or partially overlapping. In parallel, Fatheddin & Sajadian (2023) investigated the detectability of two-planet systems across a range of masses and separations, including events exhibiting either isolated or interacting planetary caustics; however, their analysis did not specifically focus on high-magnification events. In con-

¹ <https://www.jpl.nasa.gov/missions/the-nancy-grace-roman-space-telescope>

trast, the present study explicitly targets high-magnification microlensing events ($A_{\max} \gtrsim 100$), which are known to provide optimal conditions for detecting low-mass and multiple planets due to the proximity of the source trajectory to the central caustic. This focus is particularly relevant in light of the expected capabilities of the *Roman* mission, which will observe a substantial number of such events thanks to its high-cadence and high-precision photometric.

The structure of this paper is as follows. In Sect. 2, we introduce the theoretical framework of microlensing by triple-lens systems, including the relevant formalism and parametrization. In Sect. 3, we describe the simulation setup, including the generation of synthetic light curves, the noise model, and the fitting procedure. In Sect. 4, we present the results of our detectability analysis, highlighting the impact of key parameters such as mass ratios, projected separations, and source geometry. Finally, in Sect. 5, we summarize our main findings and outline future directions for extending this work.

2. Triple-Systems Events

2.1. Principles of Microlensing

Gravitational microlensing occurs when a massive object (the lens) bends the light from a background source star. The multiple images of a distant star, produced by the gravitational lensing effect, cannot be resolved due to limited angular resolution. As a result, the only observable signature is a temporary increase in the star's flux (Paczynski 1986; Mao 2012; Gaudi 2012; Tsapras 2018; Covone et al. 2000; Mroz & Poleski 2023). In the case of a triple-lens system, the lens consists of three point masses, such as a host star and two orbiting planets. This configuration leads to rich lensing behavior and complex light curves. The Einstein angle θ_E is a fundamental scale for the lensing configuration, defined as the angular radius of the Einstein ring. It is given by:

$$\theta_E = \sqrt{\frac{4GM}{c^2} \frac{D_{LS}}{D_L D_S}}, \quad (1)$$

where M is the total mass of the lensing object, D_L is the distance from the observer to the lens, D_S is the distance to the source, and D_{LS} is the distance from the lens to the source. Distances and positions in the lens plane are often measured in units of θ_E . The lens equation relates the angular position θ of an image on the sky to the true source position β :

$$\beta = \theta - \sum_{i=0}^2 \kappa_i \frac{\theta - \theta_i}{|\theta - \theta_i|^2}, \quad (2)$$

where θ_i are the angular positions of the individual lens components, and κ_i parameters are defined as $\kappa_i = \frac{\theta_E^2 M_i}{M}$, with M_i the mass of the i -th lens component, $M = \sum_i M_i$ the total lens mass. It is often useful to express the lens equation in complex notation (Witt 1990). Letting $z = (\theta_x + i\theta_y)/\theta_E$ and $\zeta = (\beta_x + i\beta_y)/\theta_E$ denote the complex positions in the image and source planes, respectively, and defining z_i as the complex positions of the lenses, the lens equation becomes:

$$\zeta = z - \sum_{i=1}^3 \mu_i \frac{1}{z - z_i}, \quad (3)$$

where $\mu_i = M_i / \sum_j M_j$ are the normalized masses, satisfying $\sum \mu_i = 1$, and the overbar denotes complex conjugation. This compact formulation is advantageous for both analytical understanding and numerical implementation. By algebraically manipulating the complex lens equation to eliminate the complex conjugate, one obtains a single-variable complex polynomial. For an N -point-mass lens, the polynomial is of degree $N^2 + 1$. According to the image theorem (Rhie 2001, 2003; Khavinson & Neumann 2006), not all roots correspond to real images: the minimum number of images is $N + 1$, while the maximum is $5N - 5$. Therefore, a triple-lens system ($N = 3$) can produce between 4 and 10 images, corresponding to the physical roots of the resulting tenth-degree polynomial. The coefficients of this polynomial depend on the normalized masses of the lenses and their complex positions. Solving this polynomial yields all possible image positions for a given source, providing a powerful method for modeling microlensing events involving three lenses.

2.2. Magnification

Each image produced by the lens contributes a magnification factor A_j , which quantifies the local brightness enhancement of the source. For a point source, this is given by the inverse of the absolute value of the Jacobian determinant of the lens mapping (Schneider et al. 1992):

$$A_j = \frac{1}{|\det J(\theta_j)|}. \quad (4)$$

The total magnification for a point source is obtained by summing over all images:

$$\mu_{\text{ps}} = \sum_j A_j. \quad (5)$$

For extended (i.e., finite-size) sources, the singularity at the caustic is smoothed out (Witt & Mao 1994), and the resulting magnification peaks become finite. Assuming a uniform surface brightness and defining the normalized source radius as $\rho = \theta_*/\theta_E$, where θ_* is the angular radius of the source star, the total magnification is given by averaging the point-source magnification over the source disk:

$$\mu_{\text{fs}}(\beta) = \frac{1}{\pi\rho^2} \iint_{|\beta' - \beta| \leq \rho} \mu_{\text{ps}}(\beta') d^2\beta', \quad (6)$$

where $\mu_{\text{ps}}(\beta')$ is the point-source magnification at position β' in the source plane.

The morphology and timescale of these smoothed magnification features depend on the source size ρ and the relative proper motion between the source and the lens, typically parameterized by the Einstein timescale t_E . The Einstein timescale is defined as $t_E = \frac{\theta_E}{\mu_{\text{rel}}}$, where μ_{rel} is the relative proper motion between the source and the lens. It represents the time required for the source to traverse an angular distance equal to the Einstein radius, and therefore provides a direct connection between the lens mass, distances, and relative motion. The sharp peaks that occur when the source crosses a caustic—known as caustic-crossing anomalies—encode detailed information about the lens configuration. These features are key to detecting and characterizing planetary companions.

To compute the total magnification, two main numerical techniques are commonly employed. The inverse ray-shooting method traces light rays backward from the observer through the lens plane, and estimates the magnification from the density of

rays reaching the source plane. While accurate and flexible, this method is computationally intensive, especially near caustics or when modeling light curves at high resolution.

An efficient alternative is the contour integration method, which computes the magnification by integrating the inverse Jacobian along the boundaries of the lensed images in the complex plane. In this work, we adopt the publicly available **VBMicrolensing** package (Bozza et al. 2025), which implements an optimized contour integration algorithm suitable for modeling complex events involving multiple lens components.

2.3. Caustics and Regimes

The set of points in the source plane where $\det J = 0$ defines the caustics (Erdl & Schneider 1993). These curves play a fundamental role in gravitational microlensing, as they mark the loci where the magnification of a point source formally diverges. Physically, this divergence corresponds to a topological transition in the lens mapping, wherein two new images are created as the source enters a caustic and two images annihilate upon exiting.

In the case of binary lenses, three principal caustic topologies are commonly distinguished—*close*, *resonant*, and *wide*—based on the projected separation s (in units of θ_E) between the two masses (Dominik 1999). Adding a second planet to a binary lens system leads to significantly more complex caustic structures (Daněk & Heyrovský 2019). A hierarchical triple-lens system composed of a host star and two planets typically exhibits a central caustic governed by the combined gravitational potential of all three masses, along with two planetary caustics whose locations depend on the projected separations (Bozza 1999, 2000b): in the wide regime, they lie near the respective planets, while in the close regime, they appear on the opposite side of the host star.

We adopt the regime classification that defines the resonant (intermediate) region based on the overlap of central and planetary caustics. Specifically, for a given mass ratio q , in the asymptotic limit of $q \rightarrow 0$, the boundaries of the resonant regime are given by:

$$s_{\min} = 1 - 0.75q^{1/3}, \quad s_{\max} = 1 + 1.5q^{1/3} \quad (7)$$

These limits define three distinct regimes: *Close* if $s < s_{\min}$; *Resonant (Intermediate)* if $s_{\min} \leq s \leq s_{\max}$; and *Wide* if $s > s_{\max}$.

This definition aligns with the behavior of planetary caustics in the low-mass ratio limit ($q \ll 1$), where the resonant regime corresponds to configurations in which the planetary caustic merges with the central one. This merging produces a single six-cusped caustic and is known as resonant lensing, enhancing perturbations near the peak of the light curve.

To classify such configurations, the binary lens nomenclature can be naturally extended to each planet individually. Each planet is assigned to one of the three regimes based on its normalized projected separation from the host star. This results in nine possible combinations of planetary configurations in a triple-lens system.

For example, in wide-wide systems, the planetary caustics are typically well-separated and produce isolated anomalies. In contrast, configurations involving at least one planet in the resonant regime—such as close-resonant or resonant-resonant systems—can yield large, connected caustics with complex internal structure, rich in observational signatures. Moreover, the interaction between the caustics of the two planets can trigger topological transitions not present in binary lenses, such as swallow-tail structures or overlapping caustic regions, as analyzed by

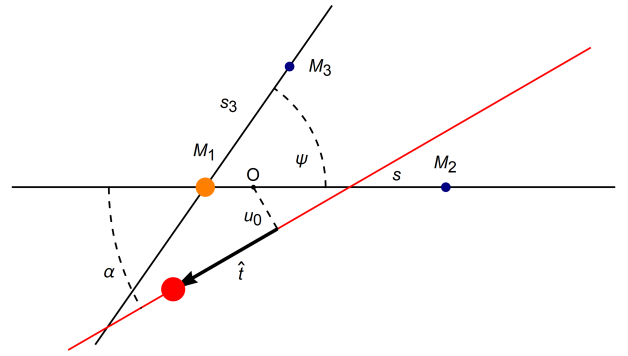


Fig. 1: Schematic convention used for the geometry of triple-lens configurations. The parameters shown in the figure are defined in Section 2.4.

Gaudi et al. (1998); Bozza (2000a); Han et al. (2001); Song et al. (2014); Daněk & Heyrovský (2015).

2.4. Parametrization

Figure 1 illustrates the geometric convention adopted for the triple-lens configuration analyzed in this work. The system consists of a primary lens (the host star) and two planetary companions. Separations are expressed in units of the Einstein angle, θ_E , and projected onto the lens plane.

The coordinate origin O is placed at the center of mass of the host star and the first planet.

The source trajectory is described by three standard microlensing parameters:

- t_0 : time of closest approach between the source and the lens system’s center of mass;
- u_0 : minimum impact parameter (in units of θ_E);
- t_E : Einstein ring crossing time.

To fully describe the lens system, we introduce the following parameters:

- q and q_3 : mass ratios of the two planets with respect to the host star;
- s and s_3 : projected separations of each planet from the host star (in units of θ_E);
- ψ : angle between the star–planet 1 axis and the star–planet 2 axis, measured counterclockwise.

We define \hat{i} as the unit vector parallel to, and oriented along, the source trajectory, indicating its direction of motion in the lens plane. The orientation of the source trajectory relative to the lens configuration is described by the angle α , defined as the angle between the source trajectory and the star–planet 1 axis.

Compared to the binary-lens case—which requires a single mass ratio q , a separation s , and a trajectory angle α —the triple-lens parametrization introduces three additional degrees of freedom: a second mass ratio q_3 , a second projected separation s_3 , and the angle ψ .

3. Simulations

3.1. Sample

To simulate realistic triple-lens microlensing events, we built upon the Galactic microlensing population framework introduced by Penny et al. (2019), employing an updated, newly

generated set of simulations made available to the authors. This dataset consists of binary-lens microlensing events produced by a host star and a single planetary companion, characterized by a planet-to-host mass ratio q and a projected separation s . Triple-lens systems were constructed by pairing two binary events with host stars of similar mass, such that the fractional difference in host star masses satisfies $|\Delta M_\star / M_\star| < 0.05$. The first event provided the base configuration (q, s) , while the second contributed a second planet (q_3, s_3) . The relative angular orientation ψ between the two planets was randomly sampled using 12 values distributed in the range $[0^\circ, 360^\circ]$, ensuring a broad range of projected configurations. In all configurations, the two planets are ordered such that $q_2 > q_3$. Although this construction method does not ensure dynamical stability, it offers an effective framework for investigating triple-lens microlensing signatures in high-magnification events.

To focus on central caustic features, we set high-magnification source trajectories with small impact parameters: $u_0 = 0.01, 0.001$, and 0.0001 . For each triple-lens configuration, we varied the trajectory angle α , measured between the source path and the host-planet 1 axis. To ensure consistency with the binary-lens analysis, we adopted the same two reference values of α used in the Penny et al. (2019) simulations.

Each model assumed a source radius ρ and Einstein timescale t_E taken from the original binary configuration. The resulting dataset consists of 1298283 synthetic light curves covering a wide variety of triple-lens geometries and observing conditions. The parameter distributions are illustrated by the light blue histogram in Figure 2.

3.2. Method

Each configuration is defined by the parameters (q, s) and (q_3, s_3) of the two planets, the orientation angle ψ , the impact parameter u_0 , and the Einstein timescale t_E and normalized source radius ρ .

Magnification curves were computed using `VBMicrolensing`, employing the `Multipoly` algorithm optimized for triple-lens systems. Each event was simulated over a 72-day observing window with a cadence of 15 minutes, consistent with the planned Roman survey (Penny et al. 2019; Zasowski et al. 2025).

To generate the observed fluxes, we combined the theoretical magnification with the photon flux expected from the source, blend, and background stars, assuming the fluxes from the Penny simulation sample and using the W149 bandpass. While Roman’s instrumental properties are well characterized, we adopted a simplified noise model to isolate the detectability of triple-lens features. Specifically, we applied Poisson noise to the simulated fluxes, drawing photon counts from a Poisson distribution at each time step. This model neglects additional detector effects such as read noise or background, but is sufficient to capture the primary photometric limitations relevant for assessing the signal strength of triple-lens signatures in high-magnification events.

To evaluate whether the presence of a second planet (i.e., the triple-lens nature of the system) could be identified, each light curve was fit with a simpler binary-lens model. The fit was performed using a non-linear least-squares minimization based on the Levenberg–Marquardt algorithm, with bounded initial conditions derived from the true configuration. We extracted the best-fit parameters and computed the binary-lens χ^2_{binary} , which was then compared to the corresponding χ^2_{triple} value obtained by evaluating the same noise-affected light curve under the original

triple-lens model (without re-fitting). In this way, the comparison isolates the improvement in fit quality attributable to the presence of the second planet. A detection was considered significant when the difference exceeded a conservative threshold of $\Delta\chi^2 = 160$, consistent with previous microlensing detection criteria (e.g., Gould et al. 2010; Suzuki et al. 2018; Penny et al. 2019).

The simulation pipeline described above enables a systematic exploration of triple-lens microlensing events across a broad range of astrophysical and geometrical configurations. By varying key parameters the framework captures the diversity of light curve morphologies that can arise in multi-planet systems. This approach allows us to probe the sensitivity of microlensing detections to the underlying lens architecture and to quantify the specific regimes in which the presence of a second planet produces statistically significant deviations from simpler binary-lens models. The resulting simulation forms the methodological basis for assessing the detectability of complex planetary configurations with Roman, and provides a direct numerical complement to previous analytical studies and detectability forecasts for multiple-planet microlensing events (e.g., Gould et al. 2010; Suzuki et al. 2018; Fatheddin & Sajadian 2023).

4. Results

In this section, we present the outcomes of our simulations aimed at evaluating Roman’s ability to uncover triple-lens microlensing systems. By analyzing the ensemble of synthetic light curves under a variety of physical and observational conditions, we quantify how often the signature of a second planetary companion can be confidently recovered. These results offer a statistical view of the parameter space where triple-lens signatures are most likely to stand out.

4.1. Global Detection Efficiency and Orbital Regime Dependence

Out of a total of $\approx 1.3 \times 10^6$ simulated light curves, we find that 66.3% satisfy our detection criterion, defined as a model fit improvement of $\Delta\chi^2 > 160$ when moving from a binary-lens to a triple-lens model. This highlights the strong sensitivity of the Roman survey to deviations introduced by multiple planets, especially when their caustic structures interact.

To explore how detectability depends on orbital configuration, we classify each event according to the projected separations s and s_3 of the two planets relative to the Einstein radius, assigning each planet to one of three regimes: *close*, *resonant*, or *wide*. This classification is based on the mass-ratio-dependent boundaries described in Section 2.3.

Table 1 presents the updated statistics using this refined classification. The results show that, in high-magnification geometries, detection efficiency is highly sensitive to whether either planet resides within the resonant zone. The highest success rates are obtained in the *s Resonant* / *s₃ Resonant* (92.8%), *s Close* / *s₃ Resonant* (91.4%), and *s Wide* / *s₃ Resonant* (89.6%) configurations — all involving at least one planet near the Einstein radius. These cases benefit from the enhanced probability that the planetary caustic overlaps with the central magnification region, particularly during the light curve peak.

In contrast, configurations where both planets lie in the wide regime (e.g., *s Wide* / *s₃ Wide*) yield lower detection rates (54.7%), reflecting the diminished central caustic influence of wide-separation planets. Intermediate success rates are observed

Table 1: Detection statistics by orbital regime

Orbital Regime	Simulated Events	Success Rate (%)	Fraction of Simulations	Detection Probability (%)	Expected Events
s Resonant / s_3 Resonant	14 518	92.82	0.01	9.32×10^{-4}	0.76
s Close / s_3 Resonant	72 472	91.37	0.06	4.58×10^{-3}	3.73
s Wide / s_3 Resonant	77 891	89.56	0.06	4.83×10^{-3}	3.93
s Resonant / s_3 Close	49 281	80.81	0.04	2.75×10^{-3}	2.24
s Close / s_3 Close	219 303	70.23	0.17	1.06×10^{-2}	8.68
s Wide / s_3 Close	263 649	69.02	0.20	1.26×10^{-2}	10.25
s Resonant / s_3 Wide	46 240	63.91	0.04	2.05×10^{-3}	1.67
s Close / s_3 Wide	258 603	55.44	0.20	9.91×10^{-3}	8.08
s Wide / s_3 Wide	294 748	54.65	0.23	1.11×10^{-2}	9.08

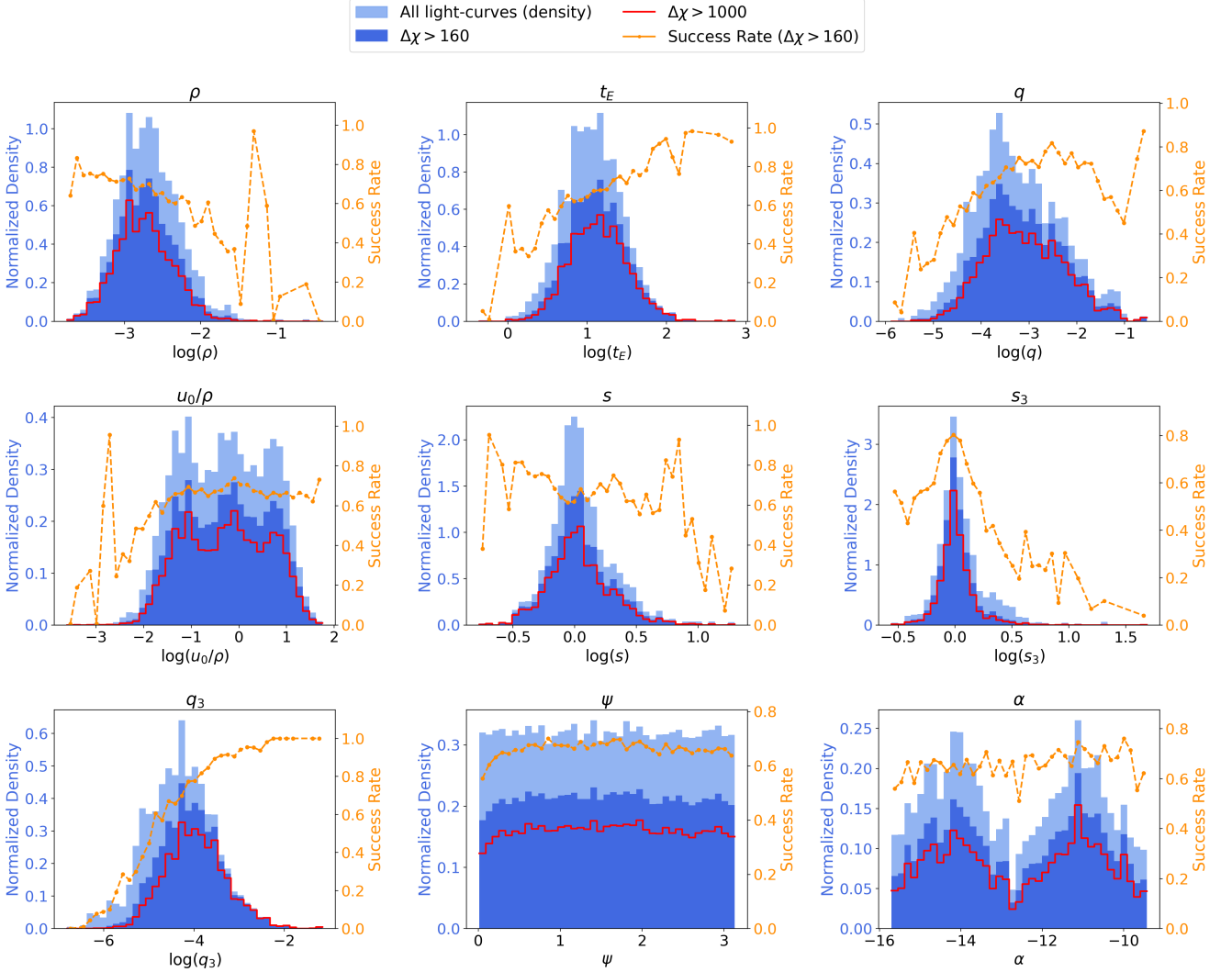


Fig. 2: Detection efficiency of triple-lens microlensing events as a function of various physical and geometric parameters. Each panel shows the normalized distribution of all simulated events (light blue), events with significant signals ($\Delta\chi^2 > 160$, dark blue), events with very strong signals ($\Delta\chi^2 > 1000$, red line), and the corresponding detection success rate (orange curve). The efficiency increases with the outer planet's mass ratio q_3 , its projected separation s_3 , and favorable source-caustic configurations.

in configurations with non-resonant separations, such as s Resonant / s_3 Close (80.8%) and s Close / s_3 Close (70.2%).

These findings confirm the dominant role of resonant caustics in enabling planetary detections in multi-lens events. Since the caustic structure is strongly dependent on both s and q , the

regime classification offers a more accurate framework to interpret detection statistics.

To place our detection efficiencies in a realistic context, we estimate the probability of detecting a high-magnification triple-lens microlensing event. According to the predictions of Penny et al. (2019), the *Roman Space Telescope* is expected to observe

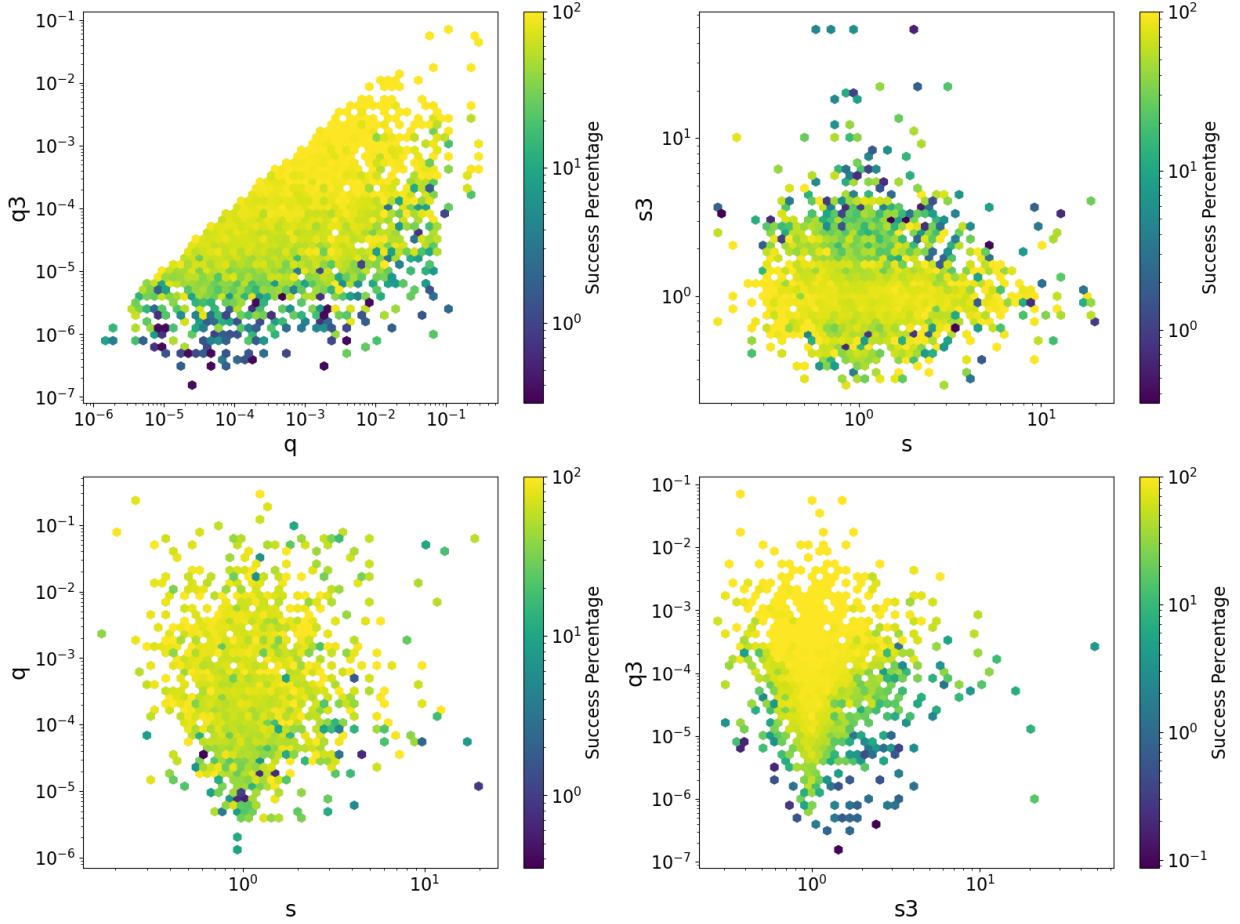


Fig. 3: Detection efficiency as a function of planetary mass ratios. The color-coded map shows the fraction of detectable triple-lens events in each (q_1, q_2) bin, where q_1 and q_2 are the mass ratios of the two planetary companions. Detection probability is highest when both planets are relatively massive ($q \gtrsim 10^{-3}$), while systems with low-mass companions ($q \lesssim 10^{-4}$) are generally undetectable. This trend reflects the dependence of caustic size and light curve anomalies on planetary mass.

approximately 54,000 microlensing events during its nominal survey, which consists of six 72-day observing seasons. Of these, about 1,400 are predicted to involve binary-lens systems with bound planetary companions, corresponding to roughly 2.6% of the total event sample. Based on our analysis of the Penny et al. sample, we find that 6.9% of these binary-lens planetary events are expected to exhibit high-magnification geometries, defined as those with $u_0 < 0.01$. For such configurations, our simulations yield an average detection efficiency of 66.3% for successfully identifying triple-lens features. Applying these factors, assuming that all simulated high-magnification binary events host an additional planet, results in an estimated detection rate of triple-lens events of approximately 4.5%, which, when multiplied by 1,400 events, corresponds to about 64 events over the course of the Roman survey. The final column of Table 1 refines this estimate for each orbital regime. Specifically, we compute the regime-dependent detection probability as the product of: (1) the probability that the event involves at least one bound planet, (2) the probability of a high-magnification configuration, (3) the regime-specific detection efficiency derived from our simulations, and (4) a normalization factor based on the relative frequency of each regime within the simulated triple-lens population.

4.2. Light Curve Morphologies Across Orbital Regimes

Figures 5–7 present representative simulated microlensing light curves for all nine orbital configurations defined by the combinations of projected separations s and s_3 , where s_3 corresponds to the less massive planet. Although these examples are not statistically representative, they offer insight into how the geometric configuration of a two-planet system influences the morphology and strength of the resulting anomaly. Figure 8 illustrates three additional cases: one in which the detection threshold of $\Delta\chi^2 = 160$ is not reached, one that marginally satisfies the threshold, and one displaying a $\Delta\chi^2$ of approximately 1000. Configurations involving a planet near the Einstein radius (*resonant regime*) typically exhibit prominent, often complex deviations centered around the peak magnification. These arise from large, centrally located caustics and frequently produce blended or multi-feature anomalies that may obscure the individual planetary contributions. In contrast, systems where both planets lie in non-resonant regimes (e.g., *Close/Close* or *Wide/Wide*) generate simpler, more isolated perturbations. These may appear as short-lived bumps or dips—often weaker and farther from the peak—due to smaller and spatially separated caustics. Mixed configurations (e.g., *Close/Resonant*, *Wide/Resonant*) often produce two temporally distinct features, one stronger anomaly near the peak from the resonant planet, and a secondary, typically

subtler signal from the non-resonant companion. The separation in time and morphology between the two features enhances the likelihood of identifying both planets individually. Overall, the figure highlights how the presence of a resonant-separation planet tends to dominate the light curve, while the lower-mass companion at s_3 contributes more localized or asymmetric perturbations. These patterns help explain the varying detectability of different orbital regimes discussed in the previous section, and provide intuitive guidance for interpreting real multiple-planet microlensing events.

4.3. Physical Implications of Detection Efficiency Trends

We begin by evaluating the effect of the source-lens impact parameter u_0 on the detectability of triple-lens events. As shown in Table 2, the detection rate remains broadly stable across the tested values of u_0 , with no significant trend emerging. The percentage of events exceeding the standard detection thresholds ($\Delta\chi^2 > 160$ and $\Delta\chi^2 > 1000$) varies only mildly, with a slight increase observed for $u_0 < 0.01$.

Table 2: Detection statistics for different u_0 values

u_0	Events with $\Delta\chi^2 > 160$ (%)	Events with $\Delta\chi^2 > 1000$ (%)
0.0001	66.23	50.35
0.0010	69.17	53.06
0.0100	63.44	46.59

To better understand how physical and geometric parameters affect detectability, we examine the histograms in Figure 2. The detectability of a second planet in a microlensing event is found to depend on the planet’s mass ratio, with only negligible sensitivity to the planets’ relative angular orientation. In particular, the histograms in Figure 2 shows that increasing the outer planet’s mass ratio q_3 boosts the triple-lens detection efficiency, whereas varying the mutual angular separation ψ between planets has little systematic effect. As expected, a larger planet-to-star mass ratio produces proportionally larger perturbations in the lens potential, yielding more extended caustics and higher magnification deviations. Consequently, massive companions (e.g. $q \gtrsim 10^{-3}$, on the order of a Jupiter/Sun ratio) generate anomalies that rise well above the photometric noise, leading to a high detection probability. By contrast, a low-mass planet ($q \sim 10^{-4}$ or below) induces only subtle caustic perturbations that often remain buried in noise and thus go undetected. The near-flat response with respect to ψ indicates that rotating the planet configuration hardly changes the total “anomaly cross-section” presented to random source trajectories. Geometrically, the overall area of the combined caustics (and thus the chance that a source will intersect a caustic) is almost invariant under rotating the lens system in the sky. Any modest changes in caustic shape due to different angles do not translate into a strong net difference in detection efficiency.

Another important factor is the Einstein crossing time t_E . As seen in the t_E panel, detection efficiency increases with event duration, especially at the short-timescale end. Events with low t_E are more likely to be missed due to poor sampling or blending with noise, whereas longer events allow for better coverage of potential anomalies and a higher probability that at least one perturbation is well sampled.

A similar trend is observed with the parameter u_0/ρ . The detection efficiency increases with this ratio, because larger values

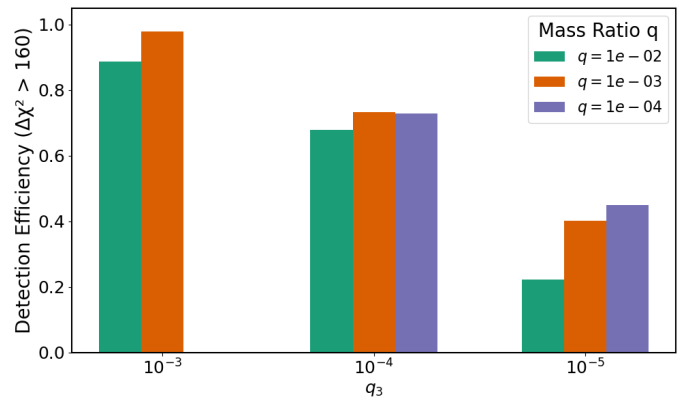


Fig. 4: Detection efficiency of a triple-lens system as a function of the mass ratio of the second planet (q_3). The efficiency is plotted for three different values of the first planet’s mass ratio ($q = 10^{-2}$, $q = 10^{-3}$, and $q = 10^{-4}$). The plot shows that when the second planet is massive ($q_3 = 10^{-3}$), the detection efficiency is high regardless of the first planet’s mass. However, as q_3 decreases, the efficiency drops, and this effect is more pronounced when the first planet is more massive.

correspond to smaller source radii ρ (for fixed u_0), which reduce finite-source smoothing. Smaller sources produce sharper caustic-crossing signatures, making the anomalies more prominent and easier to detect. Conversely, extended sources tend to smooth out the caustic features, lowering the chance of crossing a region of high magnification deviation. This behavior is consistent with what is observed in binary-lens systems, where the finite-source effect can suppress the characteristic signatures of binarity, reducing the detectability of such systems when ρ is large (Bachelet et al. 2017).

As for the source trajectory angle α , detection efficiency appears roughly constant across its full range. This flat trend reflects the near-isotropy of the magnification pattern in high-magnification events: since all considered source paths pass close to the lens center, the direction of approach has little effect on whether anomalies occur, though it may influence their shape. However, because our sample is constructed from previously detectable binary-lens events, the underlying caustic geometry tends to favor trajectories orthogonal with the binary axis, comparable to Bozza & Rota (2025). This intrinsic lens symmetry can naturally lead to a bimodal distribution in α among the events that show detectable features.

Figure 3 further shows that detection efficiency increases with the mass ratios of *both* planets. When either planet is more massive, it contributes a sizeable distortion to the lensing pattern, increasing the likelihood that at least one detectable anomaly will occur during the event. In the most favorable cases—when *both* companions are of high mass (for example, two gas giants with $q, q_3 \gtrsim 10^{-3}$)—our simulations show that nearly all such events are identifiable as triple lenses. By contrast, if both planets are in the sub- 10^{-4} mass-ratio regime, the chance of recognizing the second planet is much lower, since each produces only weak perturbations that can be masked by finite-source effects or observational noise.

The Figure 4 shows that when the second planet is relatively massive ($q_3 = 10^{-3}$), detection efficiency is nearly 100% regardless of the primary. As q_3 decreases, efficiency drops across all cases, but more steeply when the primary is more massive. Specifically, for $q = 10^{-2}$, efficiency at $q_3 = 10^{-5}$ is signifi-

cantly lower than for smaller primary planets. This is because a strong primary caustic can overshadow weak perturbations from the secondary, reducing their detectability despite being present.

As evident from Figure 2 and also from the Figure 3, and consistent with the trends discussed in Section 4.2, a key factor influencing detectability is the separation of the planets relative to the Einstein ring. Our results confirm that the probability of detecting triple systems is highest when at least one planet lies in the resonant regime ($s \sim 1$). This configuration enhances detectability by producing more distinguishable perturbations in the light curve.

In summary, the detection of triple-lens systems is primarily driven by large planet mass ratios and favorable caustic configurations. The highest efficiency is achieved when at least one planet lies near the Einstein ring and has a mass ratio $q \gtrsim 10^{-3}$. In contrast, low-mass companions, extended source sizes (large ρ), or short-duration events (low t_E) tend to produce weak or smoothed-out signals that often fall below the detection threshold. Overall, planetary mass, source size, event duration, and resonant geometry play a dominant role in shaping the success rate, while other factors such as the trajectory angle α or mutual angular orientation ψ have only a minor impact on detectability.

5. Conclusions

We have assessed the capability of the *Nancy Grace Roman Space Telescope* to detect and characterize triple-lens microlensing events—planetary systems in which two exoplanets orbit a common host star. By analyzing a large set of simulated high-magnification microlensing light curves, incorporating realistic photometric noise and Roman’s anticipated survey parameters, we quantified the conditions under which such triple-planet systems can be reliably distinguished from simpler binary-lens (single-planet) models.

Our results indicate that 66.3% of simulated high-magnification triple-lens events would be identifiable under a demanding detection threshold ($\Delta\chi^2 > 160$), demonstrating robust sensitivity to multiple-planet signatures. In favorable configurations where both planets have relatively large mass ratios (on the order of 10^{-3}), the detection success rises above 90%, whereas systems with both planets in the low-mass regime ($\sim 10^{-4}$) yield significantly lower detection rates. These trends highlight Roman’s potential to uncover a substantial population of multi-planet systems through microlensing, improving significantly upon the presently scarce detections of multiple planets by this method.

The detectability of triple-lens systems is governed primarily by the planetary mass ratios and the event geometry—in particular, the source star’s trajectory relative to the lens’s caustic structure. If the source path intersects or closely approaches the combined central caustic generated by a two-planet configuration, the resulting light-curve deviations cannot be replicated by any binary-lens model, providing a clear indication of an additional planet.

We find that the specific planetary configuration plays an important role: resonant orbital separations, particularly when the more massive planet lie near the Einstein ring, produce extended and overlapping central caustics that dominate the high-magnification region, yielding the highest detection efficiencies. In contrast, configurations in which both planets are well inside or outside the Einstein ring (e.g., close–close or wide–wide regimes) produce smaller, offset caustics that are less likely to be intersected by the source, leading to substantially lower detection probabilities.

Thus, high planetary mass ratios and resonant star–planet separations define the most favorable conditions for Roman to reveal additional planets via microlensing. Widely separated, low-mass systems with unfavorable geometry, on the other hand, are more likely to remain undetected.

Relying on the fraction of high-magnification events and our simulated detection efficiencies, we estimate that the probability of detecting a triple-lens microlensing event with *Roman* is approximately 0.1%, corresponding to around 60 events over the course of the survey. While modest, this estimate represents a significant improvement over ground-based capabilities and a promising step toward characterizing complex planetary systems.

In summary, Roman’s microlensing survey will expand the discovery space for multiplanetary systems. Roman not only will increase the detection rate of individual wide-separation exoplanets, but also will play a pivotal role in identifying systems hosting multiple planets, opening a new observational window onto planetary architectures that are inaccessible to transit and radial-velocity techniques.

Future work: Building on these results, we plan to extend our simulations to explore a broader parameter space—including varying source star radii, orbital orientations of the planets, and second-order effects such as microlensing parallax and lens orbital motion—in order to refine detectability forecasts for triple-lens systems under more diverse conditions.

References

- Auvergne, M., Bodin, P., Boissard, L., et al. 2009, *A&A*, 506, 411
- Bachelet, E., Norbury, M., Bozza, V., & Street, R. 2017, *AJ*, 154, 203
- Beaulieu, J. P., Bennett, D. P., Batista, V., et al. 2016, *ApJ*, 824, 83
- Bennett, D. P., Rhie, S. H., Nikolaev, S., et al. 2010, *ApJ*, 713, 837
- Bennett, D. P., Rhie, S. H., Udalski, A., et al. 2016, *AJ*, 152, 125
- Bennett, D. P., Udalski, A., Bond, I. A., et al. 2020, *AJ*, 160, 72
- Borucki, W. J., Koch, D., Basri, G., et al. 2010, *Science*, 327, 977
- Bozza, V. 1999, *A&A*, 348, 311
- Bozza, V. 2000a, *A&A*, 355, 423
- Bozza, V. 2000b, *A&A*, 359, 1
- Bozza, V. & Rota, P. 2025, arXiv e-prints, arXiv:2507.21309
- Bozza, V., Saggese, V., Covone, G., Rota, P., & Zhang, J. 2025, *A&A*, 694, A219
- Cassan, A., Kubas, D., Beaulieu, J. P., et al. 2012, *Nature*, 481, 167
- Chung, S.-J., Han, C., Park, B.-G., et al. 2005, *ApJ*, 630, 535
- Covone, G., de Ritis, R., Dominik, M., & Marino, A. A. 2000, *A&A*, 357, 816
- Daněk, K. & Heyrovský, D. 2015, *ApJ*, 806, 99
- Daněk, K. & Heyrovský, D. 2019, *ApJ*, 880, 72
- Dominik, M. 1999, *A&A*, 349, 108
- Erdl, H. & Schneider, P. 1993, *A&A*, 268, 453
- Fabrycky, D. C., Lissauer, J. J., Ragozzine, D., et al. 2014, *ApJ*, 790, 146
- Fatheddin, H. & Sajadian, S. 2023, *AJ*, 166, 140
- Gaudi, B. S. 2012, *ARA&A*, 50, 411
- Gaudi, B. S., Bennett, D. P., Udalski, A., et al. 2008, *Science*, 319, 927
- Gaudi, B. S., Naber, R. M., & Sackett, P. D. 1998, *ApJ*, 502, L33
- Gould, A., Dong, S., Gaudi, B. S., et al. 2010, *ApJ*, 720, 1073
- Gould, A., Udalski, A., Shin, I. G., et al. 2014, *Science*, 345, 46
- Han, C. 2006, *ApJ*, 638, 1080
- Han, C., Bennett, D. P., Udalski, A., et al. 2019, *AJ*, 158, 114
- Han, C., Chang, H.-Y., An, J. H., & Chang, K. 2001, *MNRAS*, 328, 986
- Han, C., Gould, A., Bond, I. A., et al. 2022a, *A&A*, 662, A70
- Han, C., Gould, A., Hirao, Y., et al. 2021a, *A&A*, 655, A24
- Han, C., Kim, D., Udalski, A., et al. 2020, *AJ*, 160, 64
- Han, C., Udalski, A., Choi, J. Y., et al. 2013, *ApJ*, 762, L28
- Han, C., Udalski, A., Gould, A., et al. 2017, *AJ*, 154, 223
- Han, C., Udalski, A., Jung, Y. K., et al. 2024, *A&A*, 685, A16
- Han, C., Udalski, A., Kim, D., et al. 2021b, *AJ*, 161, 270
- Han, C., Udalski, A., Lee, C.-U., et al. 2022b, *A&A*, 658, A93
- Howell, S. B., Sobeck, C., Haas, M., et al. 2014, *PASP*, 126, 398
- Johnson, S. A., Penny, M., Gaudi, B. S., et al. 2020, *AJ*, 160, 123
- Khavinson, D. & Neumann, G. 2006, *Proceedings of the American Mathematical Society*, 134, 1077, first author supported by a grant from the NSF. Communicated by Juha M. Heinonen. Published electronically: July 25, 2005
- Kuang, R., Zang, W., Jung, Y. K., et al. 2022, *MNRAS*, 516, 1704
- Kuang, R., Zang, W., Mao, S., Zhang, J., & Jiang, H. 2023, *MNRAS*, 520, 4540

- Lastovka, M., Gaudi, B. S., Johnson, S. A., et al. 2025, *AJ*, 170, 258
- Li, H., Zhang, J., Han, C., et al. 2025, arXiv e-prints, arXiv:2505.05093
- Lissauer, J. J., Ragozzine, D., Fabrycky, D. C., et al. 2011, *ApJS*, 197, 8
- Mao, S. 2012, *Research in Astronomy and Astrophysics*, 12, 947
- Mayor, M. & Queloz, D. 1995, *Nature*, 378, 355
- Mordasini, C., Alibert, Y., Klahr, H., & Henning, T. 2012, *A&A*, 547, A111
- Mroz, P. & Poleski, R. 2023, arXiv e-prints, arXiv:2310.07502
- NASA Exoplanet Archive. 2025, Planetary Systems Table, <https://exoplanetarchive.ipac.caltech.edu/>, dataset DOI: <https://doi.org/10.26133/NEA12>. Operated by the California Institute of Technology, under contract with the National Aeronautics and Space Administration under the Exoplanet Exploration Program.
- Paczynski, B. 1986, *ApJ*, 304, 1
- Penny, M. T., Gaudi, B. S., Kerins, E., et al. 2019, *ApJS*, 241, 3
- Poleski, R., Skowron, J., Udalski, A., et al. 2014, *ApJ*, 795, 42
- Rauer, H., Aerts, C., Cabrera, J., et al. 2024, arXiv e-prints, arXiv:2406.05447
- Rhie, S. H. 2001, arXiv e-prints, astro
- Rhie, S. H. 2003, arXiv e-prints, astro
- Ricker, G. R., Winn, J. N., Vanderspek, R., et al. 2015, *Journal of Astronomical Telescopes, Instruments, and Systems*, 1, 014003
- Schneider, P., Ehlers, J., & Falco, E. E. 1992, *Gravitational Lenses* (Springer-Verlag)
- Seager, S. & Mallén-Ornelas, G. 2003, *ApJ*, 585, 1038
- Shvartzvald, Y. & Maoz, D. 2012, *MNRAS*, 419, 3631
- Shvartzvald, Y., Maoz, D., Udalski, A., et al. 2017, *VizieR Online Data Catalog: Frequency of snowline-region planets* (Shvartzvald+, 2016), *VizieR Online Data Catalog: J/MNRAS/457/4089*. Originally published in: 2016MNRAS.457.4089S
- Song, Y.-Y., Mao, S., & An, J. H. 2014, *MNRAS*, 437, 4006
- Spergel, D., Gehrels, N., Baltay, C., et al. 2015, arXiv e-prints, arXiv:1503.03757
- Struve, O. 1952, *The Observatory*, 72, 199
- Sullivan, K., Dattilo, A., & Batalha, N. M. 2025, arXiv e-prints, arXiv:2511.02643
- Suzuki, D., Bennett, D. P., Sumi, T., et al. 2016, *ApJ*, 833, 145
- Suzuki, D., Bennett, D. P., Udalski, A., et al. 2018, *AJ*, 155, 263
- Terry, S. K., Bachelet, E., Zohrabi, F., et al. 2025, arXiv e-prints, arXiv:2510.13974
- Tsapras, Y. 2018, *Geosciences*, 8, 365
- Witt, H. J. 1990, *A&A*, 236, 311
- Witt, H. J. & Mao, S. 1994, *ApJ*, 430, 505
- Zang, W., Han, C., Kondo, I., et al. 2021, *Research in Astronomy and Astrophysics*, 21, 239
- Zasowski, G., Jha, S. W., Chomiuk, L., et al. 2025, arXiv e-prints, arXiv:2505.10574
- ¹⁷ Center for Research and Exploration in Space Science and Technology, NASA/GSFC, Greenbelt, MD 20771, USA
- ¹⁸ Department of Astronomy, University of California Berkeley, Berkeley, CA 94720, USA
- ¹⁹ Department of Physics and Astronomy, University of Manchester, Oxford Rd, Manchester M13 9PL, UK
- ²⁰ Department of Physics, Lehigh University, 16 Memorial Drive East, Bethlehem, PA 18015, USA
- ²¹ Las Cumbres Observatory, 6740 Cortona Drive, Suite 102, Goleta, CA 93117, USA
- ²² Observatories of the Carnegie Institution for Science, Pasadena, CA 91101, USA
- ²³ Department of Physics and Astronomy, Vanderbilt University, Nashville, TN 37235, USA
- ²⁴ Department of Earth and Space Science, Graduate School of Science, Osaka University, Osaka, 560-0043, Japan
- ²⁵ Department of Astronomy, Westlake University, Hangzhou 310030, Zhejiang Province, China
- Acknowledgements.* This work was carried out during a visiting period at IPAC, California Institute of Technology, as part of the activities of the Roman Project Infrastructure Team (PIT). VS warmly thanks the entire IPAC team for their hospitality and stimulating environment.
- VS and GC acknowledge support by the University of Napoli Federico II (project: FRA-CosmoHab, CUP E65F22000050001) and thank the university for facilitating the visiting period.
- VB acknowledges financial support from PRIN2022 CUP D53D23002590006. Funding for the Roman Galactic Exoplanet Survey Project Infrastructure Team is provided by the Nancy Grace Roman Space Telescope Project through the National Aeronautics and Space Administration grant 80NSSC24M0022, by The Ohio State University through the Thomas Jefferson Chair for Space Exploration endowment, and by the Vanderbilt Initiative in Data-intensive Astrophysics (VIDA).
- SIS's research was supported by an appointment to the NASA Postdoctoral Program at the NASA Goddard Space Flight Center, administered by Oak Ridge Associated Universities under contract with NASA.
- This research was supported in part by computational resources provided by the NASA High-End Computing (HEC) Program through the NASA Advanced Supercomputing (NAS) Division at Ames Research Center, including use of the Fornax Science Console platform developed by NASA's Astrophysics archives (IRSA, MAST, HEASARC). We gratefully acknowledge NASA for access to these resources, which made the completion of this work possible.
- We acknowledge the use of the ADHOC (Astrophysical Data HPC Operating Center) resources, within the project "Strengthening the Italian Leadership in ELT and SKA (STILES)", proposal nr. IR0000034, admitted and eligible for funding from the funds referred to in the D.D. prot. no. 245 of August 10, 2022 and D.D. 326 of August 30, 2022, funded under the program "Next Generation EU" of the European Union, "Piano Nazionale di Ripresa e Resilienza" (PNRR) of the Italian Ministry of University and Research (MUR), "Fund for the creation of an integrated system of research and innovation infrastructures", Action 3.1.1 "Creation of new IR or strengthening of existing IR involved in the Horizon Europe Scientific Excellence objectives and the establishment of networks".

¹ INAF – IAPS, Via del Fosso del Cavaliere 100, Rome, I-00133

² Dipartimento di Fisica “Ettore Pancini”, Università di Napoli Federico II, Napoli, I-80126, Italy

³ INFN – Sezione di Napoli, Via Cintia, Napoli, I-80126, Italy

⁴ Université Marie et Louis Pasteur, CNRS, Institut UTINAM UMR 6213, Besançon, France

⁵ IPAC, Caltech, 1200 E. California Blvd., Pasadena, CA 91125, USA

⁶ Dipartimento di Fisica “E.R. Caianiello”, Università di Salerno, Via Giovanni Paolo 132, Fisciano, I-84084, Italy

⁷ INAF – Osservatorio Astronomico di Capodimonte, Napoli, Italy

⁸ Department of Physics and Astronomy, Louisiana State University, Baton Rouge, LA 70803, USA

⁹ University of Canterbury, Department of Physics and Astronomy, Christchurch 8020, New Zealand

¹⁰ Space Telescope Science Institute, 3700 San Martin Drive, Baltimore, MD 21218, USA

¹¹ NASA Exoplanet Science Institute, 1200 E. California Boulevard, Pasadena, CA 91125, USA

¹² Department of Astronomy, University of Maryland, College Park, MD 20742, USA

¹³ Code 667, NASA Goddard Space Flight Center, Greenbelt, MD 20771, USA

¹⁴ Department of Astronomy, The Ohio State University, Columbus, OH 43210, USA

¹⁵ Department of Physics & Astronomy, The Johns Hopkins University, 3400 N. Charles Street, Baltimore, MD 21218, USA

¹⁶ Department of Physics, Catholic University of America, Washington, DC 20064, USA

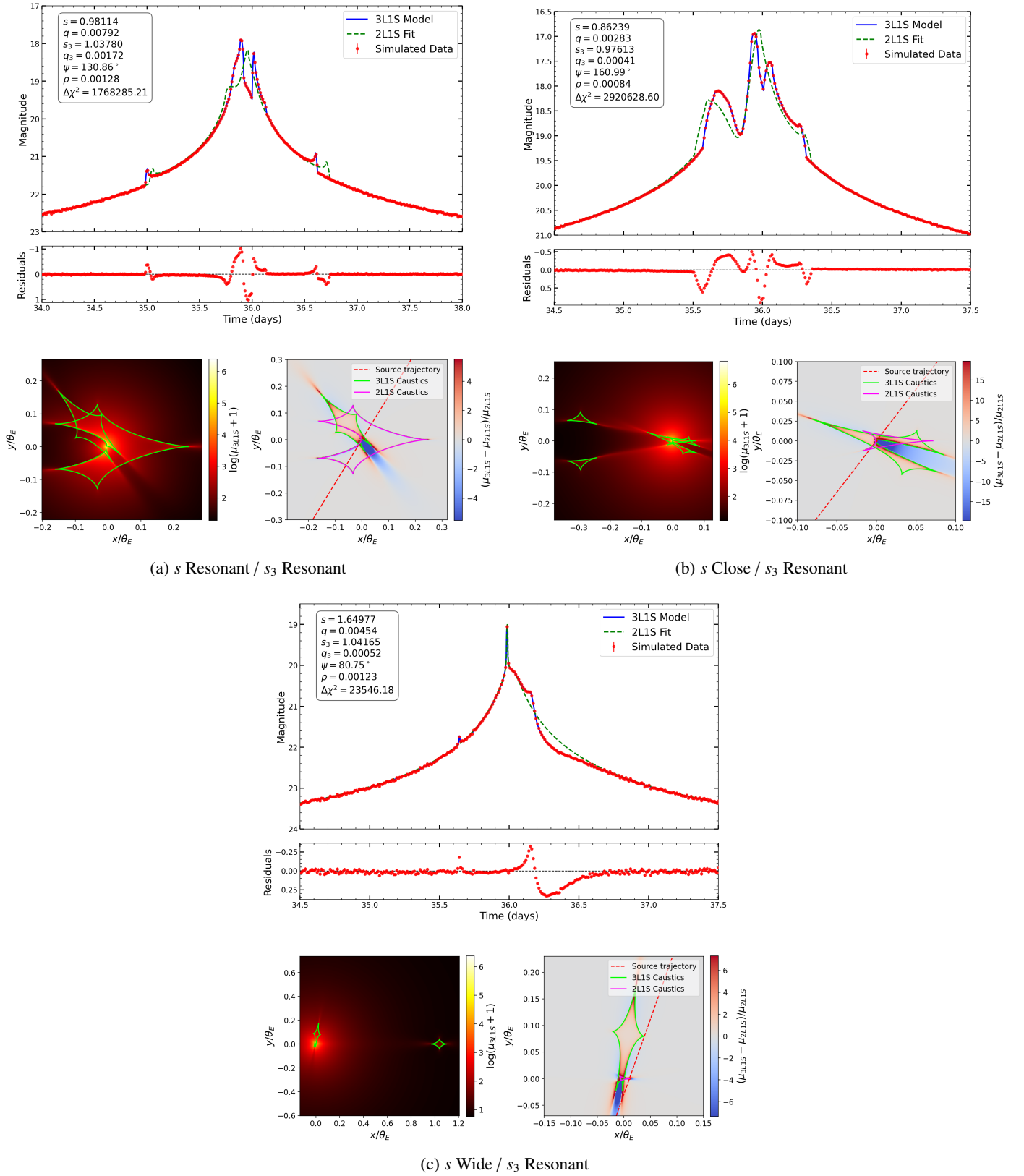


Fig. 5: Simulated light curves for triple-lens systems where at least one planet lies in the resonant regime, as defined by the mass-ratio-dependent boundaries (Equations 7). These configurations generally show strong central caustic perturbations and yield the highest detection efficiencies in our sample. For each case, the two smaller panels show the triple-lens magnification map and the map of the relative difference between the triple- and binary-lens models near the central caustic.

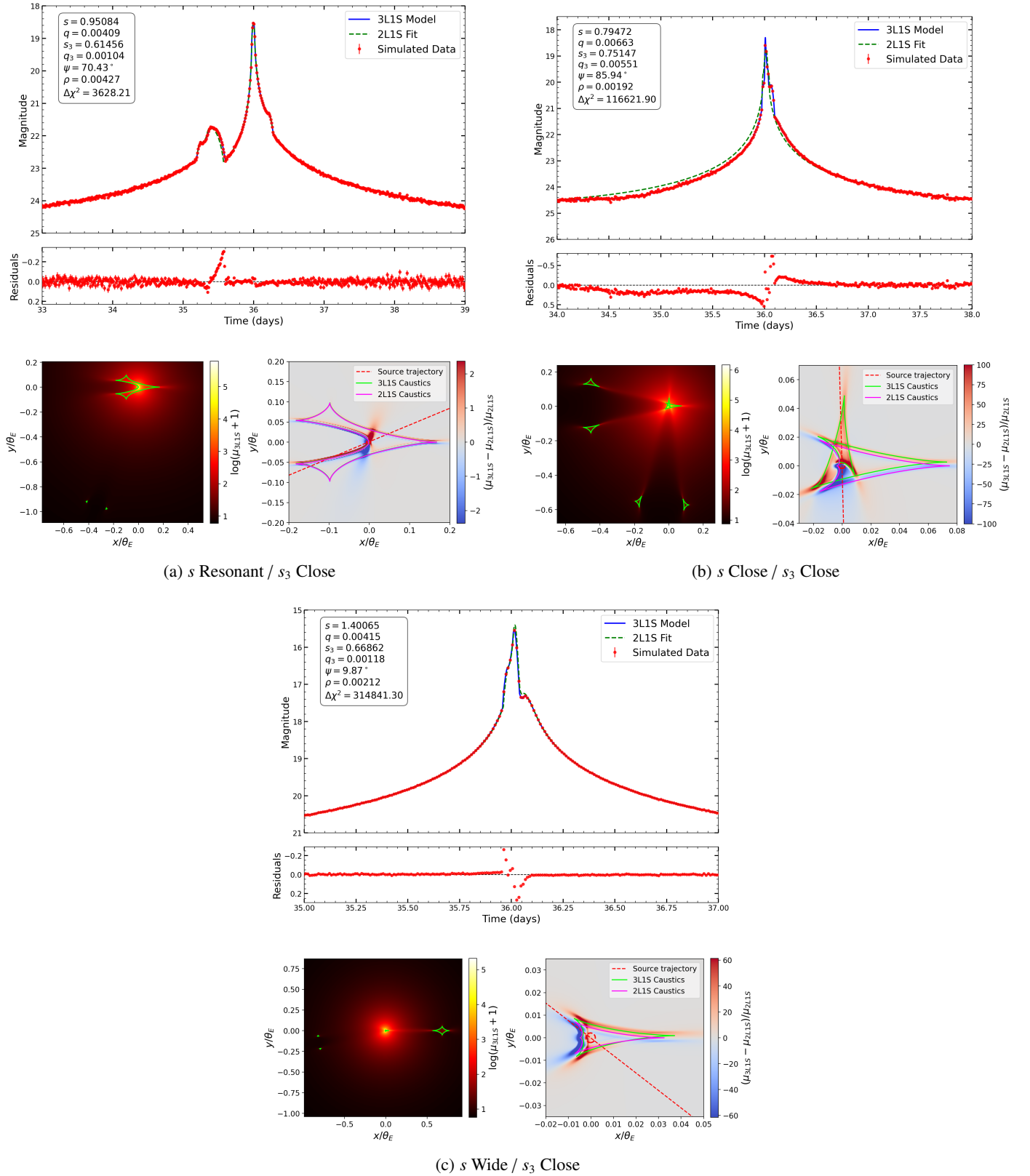


Fig. 6: Simulated light curves for configurations involving close-separation planets, or a resonant–close mix. These regimes produce intermediate detection efficiencies, with caustics that are typically more compact or asymmetric than in resonant–resonant cases. For each case, the two smaller panels show the triple-lens magnification map and the map of the relative difference between the triple- and binary-lens models near the central caustic.

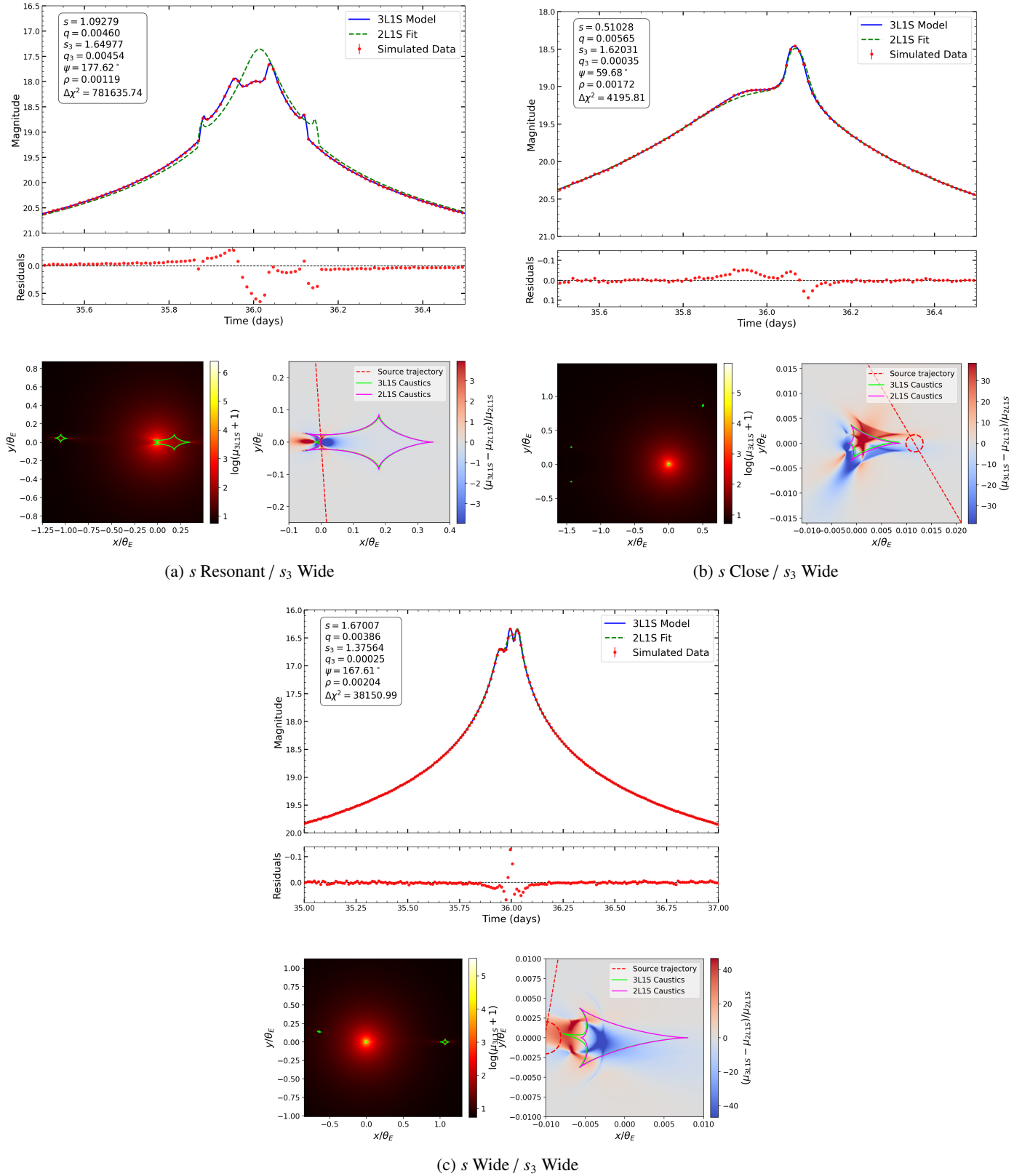


Fig. 7: Simulated light curves for orbital regimes in which at least one planet lies in the wide-separation regime. These configurations generally yield lower detection efficiencies, as planetary caustics are typically detached from the central magnification region. For each case, the two smaller panels show the triple-lens magnification map and the map of the relative difference between the triple- and binary-lens models near the central caustic.

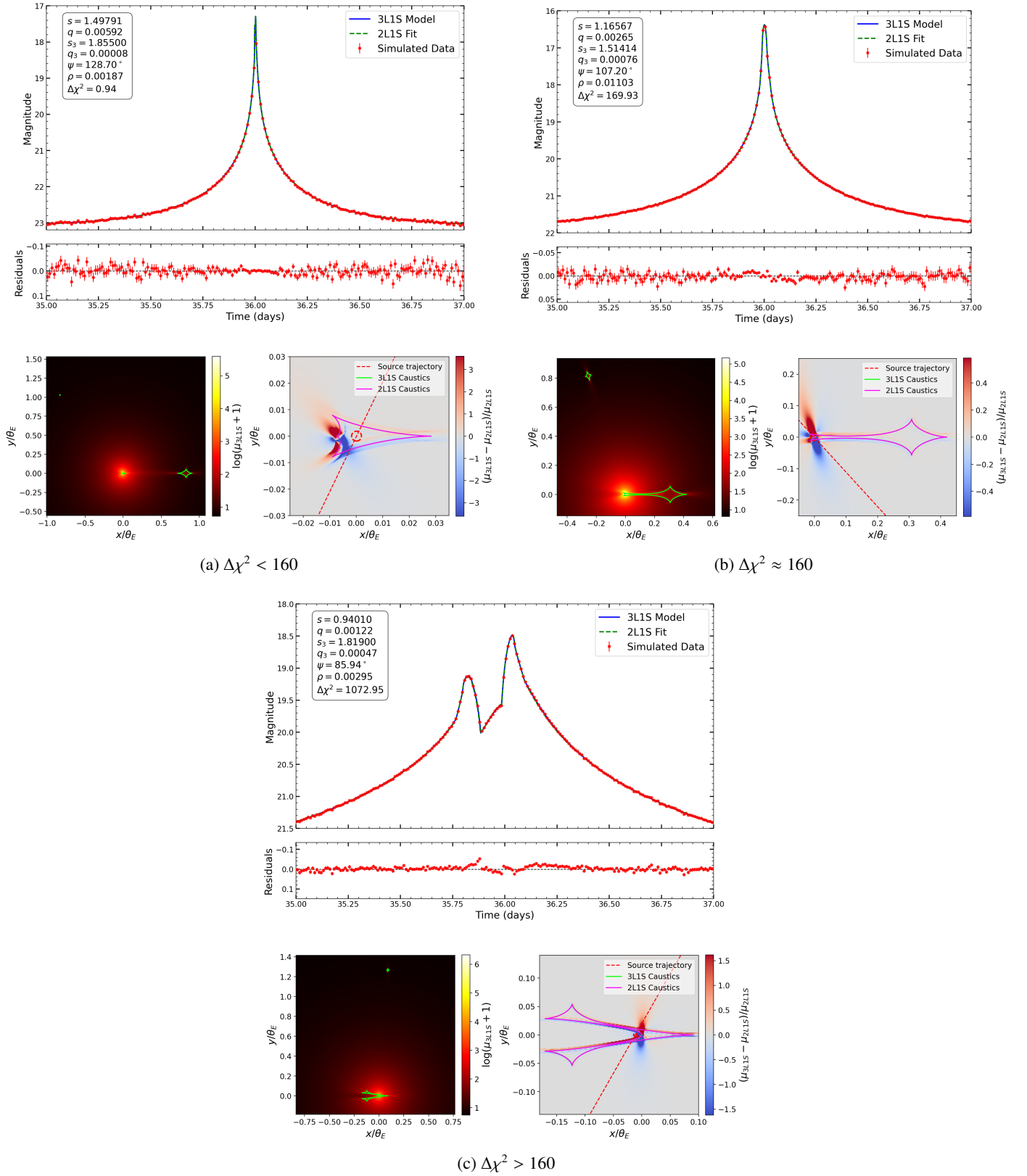


Fig. 8: Representative simulated microlensing light curves illustrating three cases with increasing detection significance. Panel (a) shows a configuration where the detection threshold of $\Delta\chi^2 = 160$ is not reached, (b) corresponds to a marginal detection near the threshold, and (c) represents a strong detection with $\Delta\chi^2 \approx 1000$. For each case, the two smaller panels show the triple-lens magnification map and the map of the relative difference between the triple- and binary-lens models near the central caustic.